VI International Conference on Computational Methods in Marine Engineering
MARINE 2015
F. Salvatore, R. Broglia and R. Muscari (Eds)

# RAIN EROSION NUMERICAL MODELING APPLIED TO MULTI-MW OFF-SHORE WIND TURBINE

**A. CORSINI*†, A. CASTORRINI*, P. VENTURINI* AND F. RISPOLI**

* Sapienza University of Rome, Dept. of Mechanical and Aerospace Engineering,
Via Eudossiana 18, 00184 Roma, Italy.
Tel: +39 0644585231

† SED Soluzioni Energia e Diagnostica Srl,
Via Asi Consortile 7, 03013 Ferentino, Italy

**Key words:** Wind turbine, rain erosion, particles cloud tracking

**Abstract.** In this work, the authors present a numerical prediction of erosion on two different blade geometry of a 6 MW HAWT designed for different aerodynamic loading, with the aim of studying their sensitiveness to erosion.

First, the fully 3D simulations are performed using an Euler-Lagrangian approach. Flow field simulations are carried out with the open-source code OpenFOAM, based on a finite volume approach, using Multiple Reference Frame methodology. Reynolds Averaged Navier-Stokes equations for incompressible flow were solved with a k-ε turbulence model.

An in-house code (P-Track) is used to compute the rain drops transport and dispersion, adopting the Particle Cloud Tracking approach (PCT). The PCT was used by some of the authors in previous works (Corsini et al., 2012; Corsini et al., 2014) to predict erosion on both axial and centrifugal fans, obtaining satisfactory results. The PCT allows to simulate a huge number of transported phase tracking just few cloud trajectories, thus resulting in reduction of computational time comparing with single particle tracking approach.

Erosion is modelled accounting for the main quantities affecting the phenomenon, which is impact velocity and angle, and material properties of the target surface.

Results provide the regions of the two blades more sensitive to erosion, and the effect of the blade geometry on erosion attitude.

## 1 INTRODUCTION

A consequence related to the increasing of offshore wind turbine size is that the wind velocity at the blade tip region reaches very high values. In normal operating conditions the tip velocity is typically between 90 and 110 m/s and in this range of velocity, the rain erosion phenomenon can have a relevant effect on the overall turbine performance. Works like [7] and [17] state that the power in case of deeply eroded leading edge can reach the 20%. Woods [2] and 3M [17] report that, in particular conditions, a serious damage on the blade leading edge can be observed after only two years of operation.

Therefore, erosion related issues should be accounted for in the scheduling of the wind turbine maintenance. This aspect becomes even more relevant in off-shore applications where, seen that the maintenance and monitoring operations must be reduced to the minimum, the rain erosion should be challenged mainly in the design phase. The use of computational tools allowing to study the erosion phenomenon in wind turbines may be of great help for

designers.

Scientific literature on this topic deals mostly about maintenance and protective coatings [6], [7]-[12], [17]. On the contrary, rain erosion in aviation is a well-known issue [4], [8], and the resistance of aircraft wings to this phenomenon is usually tested using experimental test rigs [5]. In the case of wind turbines, experiments have been performed on blade specimens and not on the whole blade [3], [6], [7].

Keegan in [1], [14] and [22], provides a complete description of the meteorological tools, experimental test cases and numerical analyses on the rain and hailstone erosion on the wind turbine blades. In particular, a FEM approach is applied to study and predict the nature and effect of raindrop and hailstone impact on wind turbine blades.

**Figure 1.** Leading edge erosion [3]

In his tests, Keegan used a blade strip, or just a part of it (namely the leading edge), evaluating the material resistance of the specimen to raindrop impacts and erosion. However, in case of very large sizes, a detailed map of the impact and damage region could help the designer through a targeted intervention on the right distribution of the protection material, which could avoid unnecessary increases in weight and costs.

The present study arises from this reasoning. Indeed, numerical solutions allow the observation of a detailed map of the three-dimensional flow field surrounding the rotor blade and, thanks to this, to predict complex phenomena like the rain impact and erosion, accounting for those three-dimensional effects that cannot be considered in the previously referred test cases.

## 2 NOMENCLATURE

**Latin**

| | | |
|---|---|---|
| R | Rotor radius | [m] |
| c | Local chord | [m] |
| k | Turbulent kinetic energy | [$m^2/s^2$] |
| P | Rotor power | [W] |
| p | Static pressure | [Pa] |
| $p_0$ | Free stream static pressure | [Pa] |
| Cl | Airfoil lift coefficient | [-] |
| Cd | Airfoil drag coefficient | [-] |
| Cp | Rotor power coefficient | [-] |
| $Re_x$ | Local Reynolds number of the blade section | |
| | $Re = V_x\, c/\nu$ | [-] |
| X, Y, Z | Absolute coordinates | [m] |

| | | |
|---|---|---|
| Ux, Uy, Uz | Air speed components | [m/s] |
| $V_0$ | Average wind speed | [m/s] |
| $Z$ | Axial coordinate | [m] |
| $X$ | Radial coordinate | [m] |
| $y^+$ | Non dimensional wall distance=$y_n u_\tau / \nu$ | [-] |

**Symbols**

| | | |
|---|---|---|
| $\nu$ | kinematic viscosity | [$m^2/s$] |
| ω | Angular velocity | [1/s] |

**Acronyms, subscripts and superscripts**

| | |
|---|---|
| CG | Centre of gravity |
| HAWT | Horizontal Axis Wind Turbine |
| MRF | Multiple Reference Frame |
| RANS | Reynolds Averaged Navier-Stokes |
| TI | Turbulence intensity |
| AoA | Angle of attack |

## 3 METHODOLOGY

The method proposed is subdivided as follows:

- Obtain the geometry of the blades through a 2D blade element momentum (BEM) based method,
- Compute the 3D steady flow around the blade with a CFD computation
- Obtain the rain droplets dynamic and interaction with the blade surface starting from the airflow solution.

The evaluation is performed on two different geometries, to have a measure of the effect that a change in geometry (in a 2D aerodynamic optimization framework) effectively could have on the specific impact pattern.

## 4 AIRFOILS AND BLADE DESIGN

The power target was selected in order to test a size that is the larger industrial state of the art. We chose to design blades, which are suitable to be mounted on a 6MW HAWT rotor with the main characteristics listed in Table 2.

The aerodynamic design process of the wind turbine blade and the performance analysis of the whole rotor are performed using the BEM method [18], the most common approach in the industry business. The chord and twist design algorithm follows a general procedure (see [37]) that is commonly used for the optimal performance design of the blade shape, in the case of a variable speed wind turbines. This was applied to find the final blade twist, in the case of linear tapered chord, and to find both chord and twist, in the case of the alternative geometry.

The algorithm consists in an iterative solution to evaluate for each section the optimal inflow angle and chord (when not constrained) as a function of the induction factors, followed by the evaluation of the optimal twist, simply by imposing the airfoil AoA of maximum aerodynamic efficiency.

For both blade geometries, the Prandtl tip and root loss corrections have been applied to the BEM model in order to obtain the final distribution of chord and twist.

In particular, for the design process a MATLAB algorithm based on the Glauert theory was developed and applied, while the performance analysis relied on the open source codes AeroDyn and FAST, both developed and distributed by the NREL [19].

Airfoil performances in different flow conditions are investigated and determined using XFOIL [20], an open source software for design and analysis of 2D subsonic isolated airfoils.

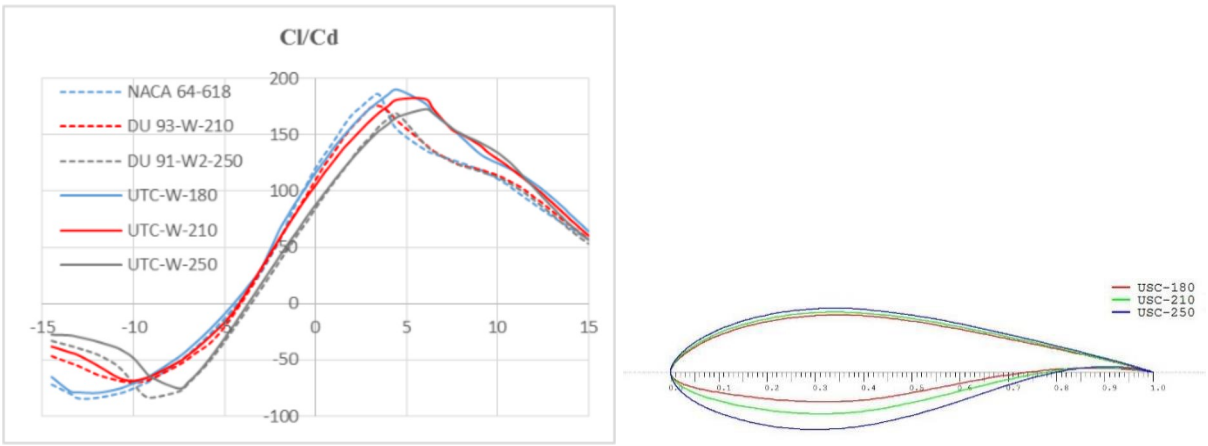


( A ) (B)

**Figure 2. A)** Airfoils aerodynamic efficiency comparison, Xfoil analysis with Re = 1.E+07, Ncrit = 9, M = 0. Continuous lines: UTC foils, dashed lines: Base foils. **B)** Optimized airfoils.

**Table 1.** Blades airfoils**.**

| **Radial position [m]** | **Baseline** | **Optimized** |
|---|---|---|
| 10.0 | DU 99-W-405 | DU 00-W2-405 |
| 17.5 | DU 99-W-350 | DU 00-W2-350 |
| 22.5 | DU 97-W-300 | DU 97-W-300 |
| 29.0 | DU 91-W2-250 | UTC-W-250 |
| 37.0 | DU 93-W-210 | UTC-W-210 |
| 46.0 – 60.0 | NACA 64-618 | UTC-W-180 |

**Table 2.** Rotor data.

| | |
|---|---|
| *Rated Wind Speed* | 12 m/s |
| *Design Rated Power* | 6000 kW |
| *Rotor radius* | 61 m |
| *Blade number* | 3 |
| *Rating rotor speed* | 15 rpm |
| *Nominal TSR* | 8 |
| *Hub radius* | 3 m |

**Figure 3.** Blade surface. Left: Baseline blade; right: Optimized airfoils blade.

Table 1 report the airfoil lists for the two geometries.
Chord and twist distributions for the second geometry were calculated applying the optimization procedure [37], this implies a non-linear chord function which reduces the blade solidity in the midspan region. To do not lose in torque, we use from the midspan to the tip, different airfoils (UTC series) which are designed to give the best performance for the particular flow conditions associated to a blade of this size.
As shown in Figure 2, the airfoils (for different maximum thickness) present geometric affinity to avoid irregularities and allow interpolation of a final surface to be as smooth as possible. Figure 2 shows also the improved performance curve of our family compared to the state-of-the-art respective ones, tested in the same flow condition (flow relative to each corresponding section of the blade).

## 5 NUMERICAL SCHEMES

### 5.1 Fluid phase solver

The flow field solution has been obtained with a CFD steady simulation of the single blade in a periodic domain. The frozen rotor approach was used to reduce the computational effort and obtain good solutions with a relatively low number of cells. In the frozen rotor simulation, the rotating and the stationary parts have a fixed relative position. A frame transformation is done to include the rotating effect on the rotating sections. This gives a steady flow and no transient effects are included.
The CFD solver used for the purpose of this work is the steady state turbulent flow solver, Semi Implicit Method for Pressure Linked Equations (SIMPLE) of OpenFOAM 2.3.x [13], which is applied to solve the RANS equations for an incompressible fluid using the Multiple Reference Frames (MRF) approach.
For this case, the tip speed value is 96 m/s, which corresponds to a Mach number of 0.266, this can assure that, in most of the fluid volume, M should have a value less than 0.3, justifying the incompressible fluid assumption. The turbulence model used in this work is the high-Reynolds number k-ε, with wall functions modeled at the wall boundary. The mean local Reynolds number measured at the blade sections ($Re_x$) is 7.785E+006 for the baseline blade, and 8.2490e+006 for the optimized blade.
Arbitrary Mesh Interface technique [23] allows the coupling of the rotating and non-rotating flow fields.

Notice that, since the simulations are running on a periodic single blade domain, we do not take into account for the tower, nacelle and ground effects. However, such complications can be avoided by supposing that the influence of these effects on the rain erosion phenomena is negligible.

### 5.2 Raindrops transport, dispersion and erosion

A Lagrangian approach is used to simulate rain drops transport, dispersion and erosion. Moreover, turbulent dispersion of droplet is modelled adopting the Particle Cloud Tracking (PCT) model, which was already used, and improved, by some of the authors in previous works [24]-[28]. This model allows to simulate a large number of droplets enclosed into a small number of particle (drops) clouds [29]-[33], thus computing only few trajectories.
In the PCT model the mean cloud position is computed by ensemble averaging the Basset-Boussinesq-Oseen (BBO) equation within a cloud. In the present study, according to literature [34], the only relevant force acting on carried phase is the drag, since the density ratio between carried and carrier phases is of the order of $10^3$, thus the ensamble average version of the BBO only accounts for this force.

$$\frac{d\langle \mathbf{v} \rangle}{dt} = \langle \beta \rangle \cdot \left[ \langle \mathbf{u} \rangle - \langle \mathbf{v} \rangle \right] \tag{1}$$

with

$$\langle \beta \rangle = \frac{3}{4 d_p} C_D \frac{\rho_f}{\rho_p} \left| \langle \mathbf{u} \rangle - \langle \mathbf{v} \rangle \right| \tag{2}$$

Droplets distribution within each cloud in the PCT model is assumed Gaussian, and it is described by the probability density function (PDF)

$$PDF(\mathbf{x}) = \frac{1}{(2\pi)^{1/2} \boldsymbol{\sigma}} \exp\left[ -\frac{1}{2} \left( \frac{\mathbf{x} - \langle \mathbf{x} \rangle}{\boldsymbol{\sigma}} \right)^2 \right] \tag{3}$$

The square root of the particle position's variance $\sigma$ is a function of the turbulent properties of the flow within the cloud

$$\boldsymbol{\sigma}^2 = 2 \left\langle \mathbf{v}'^2 \right\rangle \left[ \frac{t}{\tau_L} - \frac{1}{\tau_L{}^2} \left( 1 - e^{-t/\tau_L} \right) \right] \tag{4}$$

$\tau_L = \max\left( \tau_f, \tau_p \right)$ is the Lagrangian integral time scale, that is the maximum between the particle motion and the turbulence time scales;

$$\left\langle \mathbf{v}'^2 \right\rangle = \left\langle \mathbf{u}'^2 \right\rangle \left( 1 - e^{-\tau_f/\tau_p} \right) = \frac{2}{3} k \left( 1 - e^{-\tau_f/\tau_p} \right) \tag{5}$$

Cloud radius is assumed equal to $3\sigma$, and can varies at each time instant according to turbulent properties of the flow.

### 5.3 Rain erosion

In the recent years rain erosion on wind turbines is being studied also using computational tools. Keagan in [1] provides a review of the available models for rain erosion prediction.
According to Evans [35] a threshold damage velocity can be computed as

$$v_D \approx c_w 1.41 \left( \frac{K_t^2 c_t}{\rho_w^2 c_w^2 d_w} \right)^{1/3} \tag{6}$$

where $\rho_w$ and $c_w$ are the density of the water and the compressional wave speed in water, respectively, and $d_w$ is the droplet diameter; $K_t$ is the fracture toughness of the target material, and $c_t$ is the Rayleigh wave velocity of the target material, defined as

$$c_t = \left( \frac{0.862 + 1.14\upsilon_t}{1+\upsilon_t} \right) \left[ \frac{E_t}{2(1+\upsilon_t)\rho_t} \right] \tag{7}$$

with $\upsilon_t$ and $E_t$ being the Poisson's ratio and the Young's modulus of the target material, respectively. $\rho_t$ is the density of the target material.
The threshold damage velocity is the minimum impact velocity of a rain drop at which it provokes an erosion damage to the blade. Aiming at giving a quantitification of the damage, the threshold damage velocity has to be coupled with other quantities, since $v_D$ on its own cannot provide this information. In particular as a first approximation one can write the impact force of a droplet as [1]

$$F_i = \frac{m_w v_i^2}{d_w} \tag{8}$$

with $m_w$ representing the mass of a water droplet, and $v_i$ its impact velocity. Combining equations (6) and (8) the minimum impact force provoking damage to the blade surface, $F_D$, can be computed. Therefore, sssuming that the damage is proportional to the impact force and to the number of impacting droplets $n_w$, the damage level can be evaluated as

$$D = n_w \frac{F_i}{F_D} \tag{9}$$

In the present study we use equation (9) to evaluate the extent of damage.

## 6 PROBLEM SET UP

### 6.1 CFD Boundary conditions and numerical schemes

Table 3 show the boundary condition applied to the RANS problem. As reported, the chosen case in study corresponds to the steady 12 m/s horizontal wind, which is the nominal operating point of the selected rotor. This choice is mostly related to the will to verify that the design and especially the optimization procedures lead to a final product that effectively produces the expected performances in design operating condition.
For all the computed quantities, a second order linear upwind divergence scheme has used, setting the convergence tolerance of $10^{-7}$.

**Table 3.** Boundary conditions.

| | |
|---|---|
| *Inflow* | $V_0$ = 12 m/s; TI = 5%; |
| *Outflow* | Zero gradient |
| *Solid walls* | No-slip conditions |
| *Radial far field* | Zero gradient |

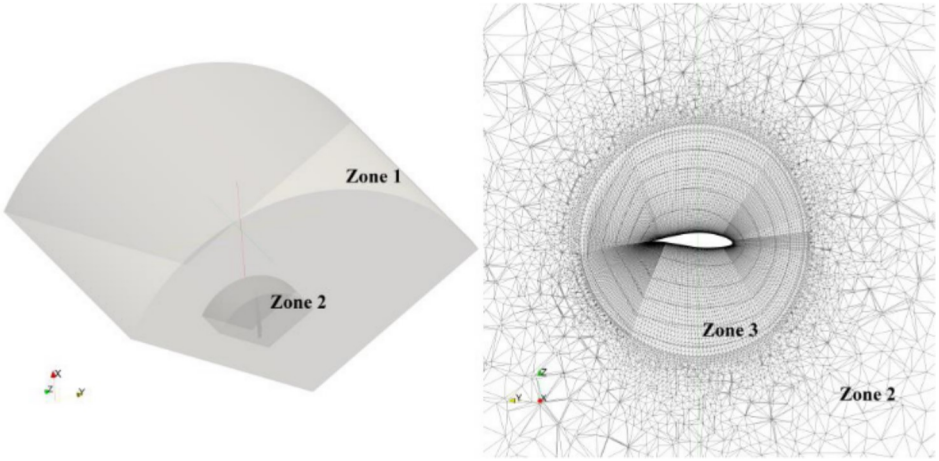


**Figure 4.** CFD grid: entire domain and slice at R = 50m of the non-inertial domain.

### 6.2 Flow field domain and numerical grid

The computational domain is a 120 degrees periodic domain subdivided in two regions in accordance with the MRF approach. In the far-field region, the code solves the flow in an inertial frame of reference, while in the rotor region the flow is solved with the addition of the non-inertial source terms to take into account the non-inertial forces. Both domains are enclosed between a couple of cyclic patches to apply the flow periodicity.

Figure  shows the overall computational domain. Three zone can be distinguished:

- Zone 1, far field domain, which has a radial extension of 240 m and a longitudinal extension of 360 m.
- Zone 2, non-inertial region that extends 4 m beyond the blade tip in the radial direction, while the two AMI patches in front and back to the rotor field are 25 meters away from the rotor disk centre.
- Zone 3 non-inertial near field region. This region is a structured mesh of hexahedral elements suitable for the solution near the boundary.

Tetrahedral elements compose both Zone 1 and 2. Table 4 reports the main mesh characteristics, while Table 5 shows a study on the solution sensitivity with respect to the grid refinement and spatial extension.

For all the domain zones the *Z* axis, which corresponds to the rotor axis, points downwind, while the X axis, which is the blade CG axis, points toward the blade tip. All the systems are coincident at the instant of the frozen rotor solution and have the origin in the hub centre.

The average values of $y^+$ ($30 < y^+ < 300$, [38]) justify the application of wall functions. A comparison, in terms of bending force and torque acting on the blade, obtained with CFD simulation and BEM simulation, is reported in Table 6.

**Table 4.** Mesh quality and $y^+$ values

| | ***Baseline blade grid*** | | | ***Optimized airfoils blade grid*** | | |
|---|---|---|---|---|---|---|
| | Minimum | Maximum | Average | Minimum | Maximum | Average |
| Volume ratio | 1 | 26.4 | 1.42 | 1 | 46.1 | 1.42 |
| Skeweness | 0.0 | 0.65 | 0.13 | 0.0 | 0.65 | 0.10 |
| Min. included angle | 7.6 | 89.6 | 52.6 | 5.1 | 89.8 | 55.3 |
| $y^+$ | 2.3 | 267.0[1] | 84.8 | 4.2 | 321.1[1] | 120.1 |
| Number of cells | 4.4M hexahedra, 4.1 tetrahedra | | | 4.3M hexahedra, 4.5 tetahedra | | |

**Table 5.** Blade torque evaluation for different grid set-up.

| **Grid type** | **Domain extension (radial, longitudinal)** | **N. of cells (nearfield)** | **Torque** kN m |
|---|---|---|---|
| Hexahedral | 1.5R, 3R | 5.5M (2.5M) | 1266 |
| Hybrid | 3R,3R | 7.5M (4.2M) | 1272 |
| Hybrid | 3R,4R | 8,5M (4.4M) | 1279 |

**Table 6.** Comparison between BEM and CFD values of bending out-of-plane force and blade torque.

| | **CFD** | **BEM** |
|---|---|---|
| Out-of-plane force *Baseline* | 280 kN | 278 kN |
| Out-of-plane force *Optimized airfoils* | 265 kN | 294 kN |
| Torque *Baseline* | 1279 kN m | 1316 kN m |
| Torque *Optimized airfoils* | 1336 kN m | 1327 kN m |

**Table 7.** Droplets and blade material properties

| | |
|---|---|
| *water density* | 100 kg/$^3$ |
| *droplet diameter* | 2 mm |
| *compressional wave speed in water* | 1490 m/s |
| *fracture toughness of epoxy material* | 1.0 MPa·m$^{1/2}$ |
| *Young's modulus of epoxy material* | 3.32 Gpa |
| *Poisson ratio of epoxy material* | 0.38 |

### 6.3 Solid phase domain and numerical grid

Motion, dispersion and raindrops erosion are computed using P-Track, an in-house FEM-based code, developed by some of the authors [24]-[28].

Since the erosion only occurs on the blade surface, there is no need of having a such large numerical domain as that used for flow field simulation. Thus, a second smaller domain is used for each blade geometry (about 1.2 M cells). These domains are structured and extend for 3 mean blade chords in the leading edge direction, and around 2 mean blade chords in other directions.

Globally 50 M droplets, each having a 2.0 mm diameter, enter the domains spread into 10 identical clouds, each cloud having a starting size of 7.5 m radius, providing a uniform raindrops distribution along the blade. The initial velocity of each cloud equals the flow velocity in the cloud mean position.

[1] The maximum y+ values are concentrated only in the final section region. This represent the 4.4E-06 of the total blade surface Furthermore, in that region a tetrahedral grid was used and the flow relative velocity is maximum.

Droplets and target material properties used in the present study are shown in Table 7.

## 7 RESULTS

A first observation comes from the flow field solution. The power output computed by integrating the aerodynamic forces (pressure forces and viscous forces) over the blade surface, confirms that, in the nominal operating point, the airfoils and blades design procedure was successful. Indeed, the computed power for both the two geometries is slightly greater than 6MW and, as reported in Table 8, the geometry with optimized airfoils produces an overall power output over 200kW greater than that produced by the baseline blade.

Figure 5 shows the final flow filed in terms of vorticity iso-surfaces, to show the near wake of the rotor. As expected, the tip vortex of the optimized airfoils blade appears less intense, while the opposite situation is observable at the blade root due to the greater value of the maximum chord.

Figure 6 collects the contour of the relative air speed magnitude at a particular radial position. The last pictures show how the optimized profiles in conjunction with the reduced chord length present a reduced trailing edge separation region, justifying the lower value of the torque due to viscous forces (Table 8). This situation can be confirmed for all the blade sections with $r > 0.2$ R.

Figure 7 shows the trajectories of the mean position of the particles cloud. It can be noticed that, the geometry with non-linear chord has a more intense secondary flow (spanwise), pushing the clouds a bit spanwise. This, together with the different swirl angle used in the two blades, is the reason for the different erosion patterns shown in Figure 8. The erosion rate was normalized by the maximum value in each simulation, thus the contour scales in Figure 8 are exactly the same. In the baseline blade, erosion is mainly concentrated on the leading edge, in particular at the tip of the blade where wind (and droplet) speed is maximum. In the second case, erosion is more spread along the blade, with a large erosion region at about midspan. This may be due to the different swirling angle comparing with the baseline, and the resulting change in velocity direction.

Separated flow conditions occur only at the blade root where the surface has cylindrical and transition profiles. Separation phenomena are mainly concentrated in the root region, however, the relative flow velocity is very low and the effect of these flow instabilities on the erosion profile is minimal.

**Table 8.** Integral aerodynamic forces and moments

| | ***Baseline blade*** | | | ***Optimize airfoils blade*** | | | |
|---|---|---|---|---|---|---|---|
| | *X* | *Y* | *Z* | *X* | *Y* | *Z* | |
| Pressure forces | 4.27 | -39.72 | 279.92 | 4.42 | -41.31 | 265.13 | kN |
| Pressure moments | -38.84 | -11069.39 | -1355.44 | -39.00 | -10551.80 | -1397.49 | kN m |
| Viscous forces | 0.06 | 1.86 | 0.38 | 0.04 | 1.64 | 0.38 | kN |
| Viscous moments | -0.41 | -11.90 | 73.73 | -0.39 | -11.23 | 60.84 | kN m |
| | | | | | | | |
| Rotor power output | | 6039.93 | | | 6298.82 | | kW |
| Rotor thrust | | 840.89 | | | 796.53 | | kN |

**Figure 5.** Vorticity iso-surface. Left: Baseline blade; right: Optimized airfoils blade.

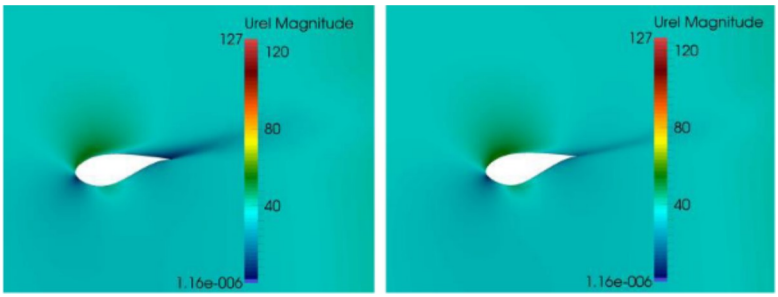


**Figure 6.** Relative velocity magnitude at 40%R. Left: baseline blade, right: Optimized airfoils blade

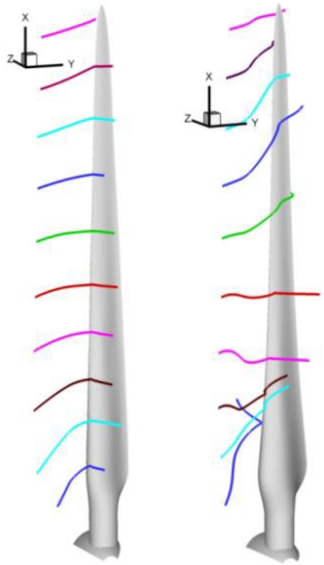

**Figure 7.** Mean position of the clouds: baseline (left) and optimized airfoils (right) blades.

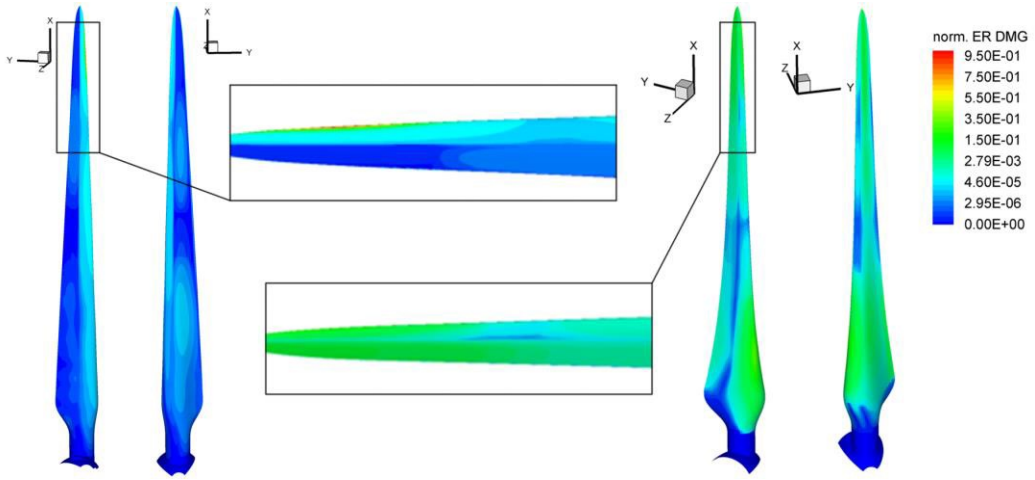


(A) (B)

**Figure 8. A)** Normalized erosion rate on the baseline blade: suction side (left), pressure side (right). **B)** Normalized erosion rate on the optimized airfoils blade: suction side (left), pressure side (right).

## 8 CONCLUSIONS

The flow-field and rain erosion of a couple of 6 MW HAWT blades were investigated. All the physics were studied by means of numerical solution, conducted using OpenFOAM for the fluid phase solution and an in house code for the droplets tracking and erosion rate prediction. For each blade geometry, authors design the aerodynamic surface and an optimization procedure on the airfoils compounding the main blade sections, was applied to obtain the second blade. The CFD computation confirms the validity of the procedure based on 2D numerical tools. Both the blades have a power output of 6MW at the rating point, that was the objective of the design phase. Furthermore, the configuration with optimized airfoils produces 4 % more power than the baseline, with the same wind and rotor radius.

Simulation of raindrop erosion put in evidence a different behaviour of the two blades. In the baseline configuration, erosion is mostly concentrated on the leading edge. This result is in agreement with what is usually observed in real applications. On the contrary, the aerodynamic behaviour of the optimized airfoils blade leads to a different impact and erosion pattern, which reflects on a larger eroded region also around the midspan of the blade. This can be due to the secondary flows generated by the non-linear chord distribution. Thus, we can conclude that both aerodynamic performance and erosion pattern should be accounted for during the design process of new geometries.

## REFERENCES

[1]. M H Keegan et al 2013. “On erosion issues associated with the leading edge of wind turbine blades”, J. Phys. D: Appl. Phys. 46 383001 doi:10.1088/0022-3727/46/38/383001

[2]. Wood K 2011 “Blade repair: Closing the maintenance gap”, Composites Technology, April

[3]. Rempel L 2012 “Rotor blade leading edge erosion – real life experiences” Wind Systems Magazine October

[4]. Gohardani O 2011 “Impact of erosion testing aspects on current and future flight conditions” Progress in Aerospace Sciences 47 280-303
[5]. University of Dayton Research Institute 2013. “Rain erosion test facility [Online].” Available: http://www.udri.udayton.edu/NONSTRUCTURALMATERIALS/COATINGS/Pages/RainErosionTestFacility.aspx [Accessed April 2013]
[6]. Haag M D 2013 Advances in leading edge protection of wind turbine blades EWEA (Vienna, Austria, 4-7, February 2013)
[7]. Powell S 2011 3M wind blade protection coating W4600 Industrial Marketing Presentation
[8]. Weigel W D 1996 Advanced rotor blade erosion protection system Kaman Aerospace Corporation, Bloomfield
[9]. TGM Services 2011 Blade erosion [Online]. Available: http://tgmwind.com/bladeerosion.html#bladeerosion [Accessed April 2013]
[10]. Henkel 2013 Blade maintenance [Online]. Available: http://www.henkelna.com/industrial/blade-maintenance-19836.htm. [Accessed March 2013].
[11]. Broadwind Energy 2012 Blade services [Online]. Available: http://www.bwen.com/WindTurbineBladeServices_7777.aspx. [Accessed March 2012].
[12]. Ropeworks 2011 Blade repair and maintenance services [Online]. Available: http://www.ropeworks.com/service_wind_blade.htm. [Accessed April 2013]
[13]. OpenFOAM packages and documentation, http://www.openfoam.org/
[14]. Keegan M H, Nash D and Stack M 2013 Numerical modelling of hailstone impact on the leading edge of a wind turbine blade EWEA (Vienna, Austria, 2013)
[15]. Haag M D 2013 Advances in leading edge protection of wind turbine blades EWEA (Vienna, Austria, 4–7 February 2013)
[16]. Rempel L 2012 Rotor blade leading edge erosion—real life experiences Wind Sys-tems Magazine
[17]. 3M 2011 A 3M study is the first to show the effects of erosion on wind turbine efficiency. Available: www.pressebox.com/pressrelease/3m-deutschland-gmbh/A-3M-Study-Is-the-First-to-Show-the-Effects-of-Erosion-on-Wind-Turbine-Efficiency/boxid/445007 (Accessed April 2013)
[18]. H. Glauerts, “Windmills and Fans”, Aerodynamic Theory (W.F. Durand, Ed.), Springer, Berlin, Germany, 1935
[19]. NWTC Information Portal (FAST v7). https://nwtc.nrel.gov/FAST7
[20]. Drela M., Youngren H., XFOIL 6.94 User Guide, Massachusetts Institute of Technology, 2001
[21]. J. Jonkman, S. Butterfield, W. Musial, and G. Scott. Definition of a 5-MW Reference Wind Turbine for Offshore System Development. Technical Report NREL/TP-500-38060 February 2009
[22]. Keegan M H, Nash D and Stack M 2012 Modelling rain drop impact of offshore wind turbine blades ASME TURBO EXPO (Copenhagen, Denmark, June 2012)
[23]. P.E. Farrell, J.R. Maddison, 2011, Conservative interpolation between volume meshes by local Galerkin projection, Computer Methods in Applied Mechanics and Engineering, 200, p. 89.

[24]. A. Corsini, A. Marchegiani, F. Rispoli, P. Venturini, A.G. Sheard, 2012, *Predicting blade leading edge erosion in an axial induced draft fan*, ASME Journal of Engineering for Gas Turbines and Power, 134, paper no. 042601.
[25]. A. Corsini, F. Rispoli, A.G. Sheard, P. Venturini, 2013, *Numerical simulation of coal fly-ash erosion in an induced draft fan*, ASME Journal of Fluids Engineering, 135, paper no. 081303.
[26]. D. Borello, P. Venturini, F. Rispoli, G.Z.R. Saavedra, 2011, *Prediction of multiphase combustion and ash deposition within a biomass furnace*, International Conference on Applied Energy, Perugia, Italy, 16–18 May.
[27]. Cardillo L., Corsini A., Delibra G., Rispoli F., Sheard A.G., Venturini P., Simulation of particle-laden flows in a large centrifugal fan for erosion prediction, ASME Turbo Expo 2014, Dusseldorf, Germany, paper no. GT2014-25865.
[28]. Corsini A., Rispoli F., Sheard A.G., Tezduyar T.E., Takizawa K., Venturini P., A variational multiscale method for cloud particle-tracking, in turbomachinery flows, Computational Mechanics, 2014 (DOI 10.1007/s00466-014-1050-0).
[29]. L.L. Baxter, 1989, *Turbulent transport of particles*, PhD thesis, Brigham Young University, Provo, UT, USA.
[30]. L.J. Litchford, S.M. Jeng, 1991, *Efficient statistical transport model for turbulent particle dispersion in sprays*, AIAA Journal, 29, pp. 1443-1451.
[31]. L.L. Baxter, P.J. Smith, 1993, *Turbulent dispersion of particles: the STP model*, Energy and Fuels, 7, pp. 852–859.
[32]. S. Jain, 1995, *Three-dimensional simulation of turbulent particle dispersion*, PhD thesis, University of Utah, Salt Lake City, UT, USA.
[33]. S.K. Kær, 2001, *Numerical investigation of ash deposition in straw-fired furnaces*, PhD thesis, Aalborg University, Aalborg, Denmark.
[34]. Crowe, C.T., Troutt, T.R., Chung, J.N., 1996, 'Numerical models for two-phase turbulent flows', Annual Review of Fluid Mechanics, vol. 28, pp. 11-43.
[35]. Evans A.G., Gulden M.E., Eggun G.E., Rosenblatt M, 1976, Impact damage in brittle materials in the elastic response regime, Rep. no. SC5023, Rockwell International Science Centre.
[36]. Li Y, Carrica PM, Paik KJ, Xing T (2012) "Dynamic overset CFD simulations of wind turbine aerodynamics". Renew Energy 37:285- 298.
[37]. Hansen M., "Aerodynamics of Wind Turbines – Second edition", Earthscan, UK, 2008
[38]. Pope S. B., "Turbulent Flows", Cambridge University Press, 2011.
[39]. Bjork, A., 1989, ''Airfoil Design for Variable rpm Horizontal Axis Wind Turbines,'' Proc., EWEC'89, Glasgow, Scotland.